Proceedings of the ASME Turbo Expo 2014
GT2014
June 16-20, 2014, Dusseldorf, Germany

GT2014-25685

COMPRESSIBLE DIRECT NUMERICAL SIMULATION OF LOW-PRESSURE TURBINES: PART I - METHODOLOGY

Richard D. Sandberg*, Richard Pichler
Liwei Chen, Roderick Johnstone
Aerodynamics and Flight Mechanics Research Group
Faculty of Engineering and the Environment
University of Southampton
Southampton, SO17 1BJ, U.K.
Email: R.D.Sandberg@soton.ac.uk

Vittorio Michelassi

Aero-Thermal Systems
GE Global Research
Munich, D-85748
Germany
vittorio.michelassi@ge.com

ABSTRACT

Modern low pressure turbines (LPT) feature high pressure ratios and moderate Mach and Reynolds numbers, increasing the possibility of laminar boundary-layer separation on the blades. Upstream disturbances including background turbulence and incoming wakes have a profound effect on the behavior of separation bubbles and the type/location of laminar-turbulent transition and therefore need to be considered in LPT design. URANS are often found inadequate to resolve the complex wake dynamics and impact of these environmental parameters on the boundary layers and may not drive the design to the best aerodynamic efficiency. LES can partly improve the accuracy, but has difficulties in predicting boundary layer transition and capturing the delay of laminar separation with varying inlet turbulence levels. Direct Numerical Simulation (DNS) is able to overcome these limitations but has to date been considered too computationally expensive. Here a novel compressible DNS code is presented and validated, promising to make DNS practical for LPT studies. Also, the sensitivity of wake loss coefficient with respect to freestream turbulence levels below 1% is discussed.

NOMENCLATURE

E	total energy
J	Jacobian grid matrix
M	Mach number
Re	Reynolds number
Pr	Prandtl number
T	temperature
a	speed of sound
c_p	static pressure coefficient, specific heat
C	chord length
q	heat flux
u,v,w	velocity components
$x_\xi, x_\eta, y_\xi, y_\eta$	grid metrics
y^+	coordinate in wall-scaling
γ	ratio of specific heats
κ	thermal conductivity
μ	molecular viscosity
ϕ	phase shift
ρ	density
τ	viscous stress
Θ	wavenumber
Sub and Superscripts	
$_2$	exit plane
$_{ax}$	axial
$_{is}$	isentropic
$_\infty$	reference value
*	dimensional value
Abbreviations	
HPC	High-performance computing
OMP/MPI	Open Message Passing / Message Passing Interface

INTRODUCTION

To reduce specific fuel consumption and cost of jet engines, the aerodynamic load of modern low pressure turbines (LPT), as measured by the Zweifel number, is increasing on account of both a growth in lift and a blade count decrement. As a result the suction side boundary layer is longer exposed to increasingly large adverse pressure gradients.

At the same time, chord Reynolds numbers are moderate as a consequence of small chord-size of the blades and their operation in low air density environments. This combination results

*Address all correspondence to this author.

in the suction and pressure side boundary layers becoming prone to laminar separation and subsequent laminar-turbulent transition of the separated shear layers [1, 2]. Separation bubbles and the type and location of laminar-turbulent transition are sensitive to upstream disturbances, including background turbulence in the main stream and wakes from the upstream rows [3, 4]. As the profile losses depend strongly on the state of the boundary layers on the blades [5], it is crucial that the boundary layer states can be predicted accurately in order for LPT design to match stringent performance and weight requirements. Although Reynolds Averaged Navier–Stokes (RANS) incorporating the latest transition models appear to achieve good agreement with experiments at low Reynolds numbers in terms of pressure coefficient and transition onset, these models are often unable to provide accurate results in terms of total pressure losses [6] in the wide design space generally required for changing operating conditions of LPT. Also RANS are often found inadequate to resolve the complex interactions of periodic inflow perturbations, often combined with large background turbulence intensity, with the boundary layers.

Large Eddy Simulation (LES) have therefore been used for numerical studies of low-pressure turbines [7–9], owing to the improved accuracy achieved by resolving the energy-containing structures in the flow while keeping computational cost at bay by modeling the small scales of turbulence. However, LES suffers from difficulties in predicting boundary layer transition and capturing the delay of laminar separation with varying inlet turbulence levels [10], or due to periodic incoming wakes [11].

To remove any uncertainty incurred by use of turbulence modeling, Direct Numerical Simulation (DNS) can be considered. DNS solves the fully nonlinear, time-dependent Navier-Stokes equations without any empirical closure assumptions, and by specifying initial and boundary conditions precisely controlled 'numerical experiments' of a physical problem can be conducted. Such numerical experiments have over the past decades provided data not obtainable by traditional laboratory experiments and have helped gain insight into fundamental mechanisms in fluid mechanics, for example in near-wall turbulence [12]. DNS data have also been heavily used for developing, validating, or improving turbulence models [13]. However, as DNS needs to resolve all length and time scales of turbulence, the computational cost can be shown to increase approximately as Re^3 [14] and numerical challenges need to be overcome [15]. Therefore, initially, only highly idealized configurations, artificially small computational domains and low Reynolds numbers were considered. However, as the available computing power has increased tremendously since the first use of DNS, more realistic Reynolds numbers and of more practical flows and geometries have become possible.

The first numerical simulations that fully resolved transition to turbulence within a laminar separation bubble were conducted by Alam & Sandham [16] and Spalart & Strelets [17]. The two studies considered separation bubbles on a flat plate, induced by upper boundary transpiration, and apparently observed different instability mechanisms leading to transition, and different transitional behavior. The first DNS study of compressible separation bubbles on airfoils was conducted by Jones *et al.* [18] in which a transition mechanism independent of upstream disturbances was found. The first incompressible DNS of a turbine cascade was performed by Wu & Durbin [19] and found evidence that incoming wakes are responsible for longitudinal structures forming on the pressure side. Additional incompressible DNS have contributed further to the understanding of the effect of incoming wakes on the pressure and suction side boundary layers [20–22]. Nevertheless, the Reynolds numbers tackled with DNS so far have been relatively low and to date there have been no compressible DNS of LPT cascades, despite the observation by Wissink [21] that the pressure distribution of incompressible calculation is not comparable to the pressure distribution of compressible experiment because incompressible simulations of compressible measurements yield an anticipated and stronger peak suction. Furthermore, if the aim is to support and guide the LPT design process, DNS needs to shed its character of being a 'heroic' undertaking, i.e. vast computational resources are expended for simulations with only one, or a very limited, set of parameters. On the contrary, DNS needs to be sufficiently affordable to allow for parameter sweeps at meaningful Reynolds numbers. The prerequisite for this is the availability of a numerical code that can fully exploit the latest computer hardware.

This paper makes three contributions. Firstly, it demonstrates that a Navier–Stokes solver purposely developed to exploit modern HPC architectures enables DNS of LPT configurations at sufficiently short wall time that parameter sweeps become feasible. The key ingredients for an efficient algorithm are presented, followed by a performance study and a thorough validation against benchmark data for canonical flows. Secondly, the article shows that compressible DNS of linear LPT cascades show excellent agreement with laboratory experiments. Thus numerical experiments, as presented here and in the accompanying Part II of the paper, can be relied upon. Finally, it is shown that wake losses are highly sensitive to inlet turbulence levels even at disturbance levels below 1% and that therefore even disturbance levels of nominally 'clean' experiments need to be known and replicated in DNS for results to agree with experimental data.

NUMERICAL METHOD

The main objective for the development of the in-house multi-block structured curvilinear compressible Navier–Stokes solver HiPSTAR (High Performance Solver for Turbulence and Aeroacoustics Research) was performance and accuracy. The algorithm has been designed with maximum efficiency, i.e. minimal runtime for a given accuracy, in mind to allow cutting-edge large-scale computer simulations on today's High Performance Computer (HPC) systems and to minimize computation time for a given problem to make best use of the available resources. In the following, the key ingredients for achieving these goals are given.

Algorithm

One of the most effective ways to increase the performance of a numerical code on a HPC system is to reduce the memory requirement of a simulation for a given problem. For typical DNS, the size of the simulations exceeds the available cache of the CPUs such that RAM needs to be accessed. Because of the very high clock-speeds of current CPUs, for modern HPC systems,

memory access is the limiting factor in the total performance of simulations and not the number of operations to be performed. Minimizing the allocated memory can be achieved by both reducing the grid-cell count required to spatially resolve the flow under consideration, or by improving the efficiency of the algorithm so that a smaller number of arrays need to be allocated.

To satisfy the latter requirement, a five-step, fourth-order accurate Runge–Kutta scheme [23] was implemented because of its ability to achieve fourth-order accuracy with only two registers of memory. In order to increase the robustness of the numerical scheme for the direct numerical simulations and to avoid aliasing errors of the cubically nonlinear convective terms within the discretized Navier–Stokes equations, a conditioning of the compressible Navier–Stokes equations according to [24] was implemented. This (optional) method employs skew-symmetric splitting of the non-linear terms, but, unlike in previous methods, quadratic and cubic nonlinearities are split differently. For all DNS of LPT configurations discussed in this paper, the skew-symmetric splitting was enabled.

Another low-memory ingredient is that only the streamwise (axial) and lateral (pitchwise) coordinate system (x,y) is mapped to general coordinates (ξ,η). By deliberately restricting the coordinate mapping to two dimensions, the spanwise grid is independent of the other two coordinate directions, e.g. full three-dimensional curvilinear simulations are not possible. What might seem as a profound constraint is advantageous in two ways: firstly an efficient spectral method can be employed for the discretization of the spanwise direction, and secondly a smaller number of metric terms is required than for the most general case, and all metric terms needed in the current case are two-dimensional (versus three-dimensional if a mapping was performed in all coordinate directions). Therefore much less memory is required for the simulations.

Generalized curvilinear coordinates In HiPSTAR, the flow is assumed to be an ideal gas with constant specific heat coefficients and all quantities were made dimensionless using the flow quantities at a reference location in the flow denoted by subscript ∞. In the case of LPT simulations, the blade chord-length is chosen as the reference length. The non-dimensionalization results in the following dimensionless parameters:

$$Re = \frac{\rho^*_\infty u^*_\infty C^*}{\mu^*_\infty} \qquad M = \frac{u^*_\infty}{a^*_\infty} \qquad Pr = \frac{\mu^*_\infty c^*_p}{\kappa^*_\infty}$$

With x,y,z denoting the axial, pitchwise and spanwise directions, respectively, and u,v,w denoting the velocity components in the x,y,z directions, respectively, the non-dimensional compressible Navier–Stokes equations in conservation form as solved by HiPSTAR in mapped computational space ξ,η,z are

$$\frac{\partial \hat{\mathbf{Q}}}{\partial t} + \frac{\partial \hat{\mathbf{E}}}{\partial \xi} + \frac{\partial \hat{\mathbf{F}}}{\partial \eta} + J\frac{\partial \mathbf{G}}{\partial z} = \frac{\partial \hat{\mathbf{E}}_\mathbf{v}}{\partial \xi} + \frac{\partial \hat{\mathbf{F}}_\mathbf{v}}{\partial \eta} + J\frac{\partial \mathbf{G}_\mathbf{v}}{\partial z} \qquad (1)$$

where the conservative variable and the inviscid flux vectors in generalized coordinates are given as

$$\hat{\mathbf{Q}} = J\mathbf{Q} \qquad \hat{\mathbf{E}} = y_\eta \mathbf{E} - x_\eta \mathbf{F} \qquad \hat{\mathbf{F}} = -y_\xi \mathbf{E} + x_\xi \mathbf{F}$$

and the viscous flux vectors in generalized coordinates are

$$\hat{\mathbf{E}}_\mathbf{v} = y_\eta \mathbf{E}_\mathbf{v} - x_\eta \mathbf{F}_\mathbf{v} \qquad \hat{\mathbf{F}}_\mathbf{v} = -y_\xi \mathbf{E}_\mathbf{v} + x_\xi \mathbf{F}_\mathbf{v}$$

The conservative variable and the inviscid flux vectors are

$$\begin{aligned}
\mathbf{Q} &= [\rho,\, \rho u,\, \rho v,\, \rho w,\, \rho E]^T \\
\mathbf{E} &= [\rho u,\, \rho uu + p,\, \rho uv,\, \rho uw,\, u(\rho E + p)]^T \\
\mathbf{F} &= [\rho v,\, \rho uv,\, \rho vv + p,\, \rho vw,\, v(\rho E + p)]^T \\
\mathbf{G} &= [\rho w,\, \rho uw,\, \rho vw,\, \rho ww + p,\, w(\rho E + p)]^T
\end{aligned}$$

with the total energy $E = T/[\gamma(\gamma-1)M^2] + 1/2 u_i u_i$ and $\gamma = 1.4$. The viscous flux vectors are

$$\begin{aligned}
\mathbf{E}_\mathbf{v} &= [0,\, \tau_{xx},\, \tau_{xy},\, \tau_{xz},\, -q_x + u\tau_{xx} + v\tau_{xy} + w\tau_{xz}]^T \\
\mathbf{F}_\mathbf{v} &= [0,\, \tau_{yx},\, \tau_{yy},\, \tau_{yz},\, -q_y + u\tau_{yx} + v\tau_{yy} + w\tau_{yz}]^T \\
\mathbf{G}_\mathbf{v} &= [0,\, \tau_{zx},\, \tau_{zy},\, \tau_{zz},\, -q_z + u\tau_{zx} + v\tau_{zy} + w\tau_{zz}]^T
\end{aligned}$$

with the stress tensor and the heat-flux vector computed as

$$\tau_{ik} = \frac{\mu}{Re}\left(\frac{\partial u_i}{\partial x_k} + \frac{\partial u_k}{\partial x_i} - \frac{2}{3}\frac{\partial u_j}{\partial x_j}\delta_{ik}\right) \quad q_k = \frac{-\mu}{(\gamma-1)M^2 PrRe}\frac{\partial T}{\partial x_k} \qquad (2)$$

respectively, assuming the Prandtl number to be constant at $Pr = 0.72$. The molecular viscosity μ is computed using Sutherland's law [25], setting the ratio of the Sutherland constant over freestream temperature to 0.36867. To close the system of equations, the pressure is obtained from the non-dimensional equation of state $p = (\rho T)/(\gamma M^2)$.

Spatial Discretization To minimize the number of total grid-cells required for accurate simulation of a given problem, the spatial discretization is performed with a Fourier method (using the FFTW3 library) in the spanwise direction and a novel wave-number optimized compact finite-difference scheme with near-spectral accuracy for the axial and pitchwise directions. These schemes offer low dispersion and dissipation errors and are therefore a logical choice for long-time accurate simulations of hydrodynamic instabilities, laminar-turbulent transition and turbulence, as the high-wavenumber errors are kept to a minimum. The compact schemes used in HiPSTAR are novel in that they can be parallelized efficiently [26]. In Fig. 1 the modified wavenumber of the novel scheme is plotted and compared with the exact solution obtained using spectral methods and traditional, non-optimized high-order standard and compact finite-difference schemes. It can be observed that the 4^{th}-order accurate wavenumber optimized compact finite-difference scheme shows very good wavenumber resolution characteristics, with the first

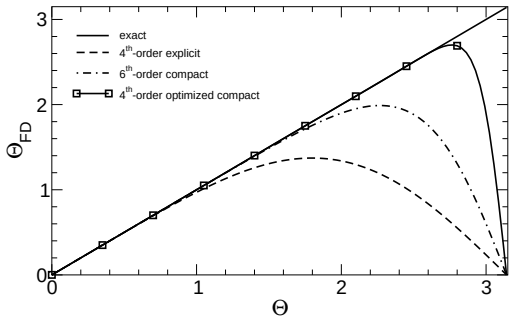

FIGURE 1. MODIFIED WAVENUMBER OF THE PARALLEL COMPACT SCHEME USED IN HiPSTAR [26], COMPARED WITH TRADITIONAL NON-OPTIMIZED STANDARD AND COMPACT SCHEMES.

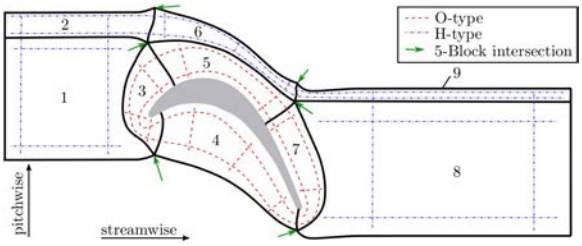

FIGURE 2. COMBINED O-TYPE/H-TYPE GRID TOPOLOGY TYPICALLY USED FOR LINEAR CASCADE SIMULATIONS.

deviation from the exact solution at $\Theta \simeq 2.7$, a factor of 2.7 higher than a standard 4^{th}-order explicit scheme. This implies that the grid can be coarser by the same factor while still resolving the same flow features, which more than outweighs the additional cost of having to solve a penta-diagonal matrix system for each MPI process.

Complex Geometries For studies of flows over blades in linear cascades, it is desirable to allow for the combination of an O-type grid around the blade, enabling adequate resolution at leading and trailing edges, and an H-type grid away from the blade to allow for pitchwise periodic boundary conditions. When coupling O- and H-type grids, it is unavoidable that the metric terms at intersecting block boundaries become discontinuous. To avoid spurious errors that would result when applying central finite-difference schemes across these interfaces with metric discontinuities, characteristic interface conditions (CIC) [27] are used for the coupling of the blocks. As the governing equations are solved in general curvilinear coordinates, either the ξ or η coordinate in computational space is normal to the block interfaces and the characteristic decomposition of the flow in the normal direction to the interface is straightforward. In Fig. 2 a typical 9-block set-up for a linear turbine cascade is shown, with the O-type grid comprising blocks 3, 4, 5 and 7 and the H-type grid the remaining 5 blocks. Each block can then in turn be broken down into sub-domains, as indicated by dashed lines, each allocated to an MPI process, for more efficient parallelization, as discussed below.

Inflow Turbulence To study the sensitivity of linear turbine cascade flow to inflow turbulence, a turbulent inflow generation technique is required. Experimental studies mostly provide turbulent intensities and some also give length scales. In general, only these two parameters are available from real turbomachinery data as well. Thus the turbulence generation method has to allow to adjust these parameters to mimic both experiments and real turbomachinery flow. A quantitative description of turbulence in experiments has been reported by, e.g., Michálek *et al.* [28]. In addition to the turbulence intensities they also quantified the homogeneity to be $\overline{u^2}/\overline{v^2} = 1.2$. Also they reported length scales to be slightly above 10% of the chord length which might require spanwise domain sizes in excess of what is required to resolve the actual flow about a blade. Therefore, a value of about 5% is targeted in this study.

Various methods to generate turbulence have been proposed and were reviewed by Tabor *et al.* [29]. Two main methods have evolved: ones that read in turbulence data (file-IO heavy), and another group that synthetically generates turbulence. IO heavy methods generally are a bottleneck in terms of computational efficiency and thus initially a digital filter approach [30] was adopted in the current study to produce homogeneous inlet turbulence [31]. However, it was found that the inflow generation technique increased the overall computational cost by approximately $\sim 30\%$ when selecting the turbulent length scales to the desired values of about 5% of chord. For that reason, another, computationally more efficient approach, was developed for the current study. For LPT simulations a inlet domain length of at least 80% chord is required to obtain the correct potential flow, thus a simple method, based on harmonic waves at a few discrete wave numbers, can be considered despite possibly requiring a longer development length for the turbulence than more sophisticated, but more expensive, methods. Perturbations are introduced in the three velocity components at the inlet using a sum of n discrete waves of the form

$$\begin{aligned} u'(n,t,y,z) &= c_1(n)\sin[f(n,t)]\cos[g(n,t,y)]\cos[h(n,t,z)] \\ v'(n,t,y,z) &= c_2(n)\cos[f(n,t)]\sin[g(n,t,y)]\cos[h(n,t,z)] \\ w'(n,t,y,z) &= c_3(n)\cos[f(n,t)]\cos[g(n,t,y)]\sin[h(n,t,z)] \end{aligned} \quad (3)$$

The arguments of the harmonic functions in time t (and through convection in the streamwise direction x), the pitchwise y and spanwise z directions are given by

$$\begin{aligned} f(t,n) &= \beta_1(n)t + \varphi_1(n) \\ g(t,y,n) &= \beta_2(n)(y - \dot{\phi}_2(n)t) + \varphi_2(n) \\ h(t,z,n) &= \beta_3(n)(z - \dot{\phi}_3(n)t) + \varphi_3(n) \end{aligned} \quad (4)$$

Each of the parameters in equations 4 and 5 allows fine-tuning of the inlet perturbations to obtain a turbulence target state. The time and length scales can be adjusted using the frequencies $\beta_1(n)$ and the wave numbers $\beta_2(n)$ and $\beta_3(n)$. The computational domain is periodic in the pitchwise and spanwise directions requiring that the wave numbers have to be chosen such that the perturbations satisfy the same constraint. This is realized by re-

quiring

$$\beta_{2,3}(n) = 2\pi \frac{k_{2,3}(n)}{p_{2,3}} \tag{5}$$

where p_2 and p_3 are the pitchwise and spanwise length, respectively, and $k_{2,3}$ are integers. Note that the spanwise and pitchwise wave numbers are in general not the same. This limitation does not apply to $\beta_1(n)$. Different orientations of the inlet structures can be achieved by adjusting $\dot{\phi}_i(n)$. Finally a phase shift can be specified using $\varphi_i(n)$. The turbulence intensities are adjusted using the coefficients c_i independently for each direction. In an exhaustive preliminary study, it was found that good results were obtained using a total of 16 waves, based on four different wave number combinations j. The wave numbers for each j are given in the left part of table 1. Each wave in each of the wave number combinations j is shifted by one fourth of a period and the corresponding $\dot{\phi}_i$ are given in the right part of table 1.

TABLE 1. TURBULENCE GENERATION PARAMETERS.

j	β_1	k_2	k_3	n	$\dot{\phi}_2$	$\dot{\phi}_3$
1	10.90	4	1	1	0	u
2	17.35	7	3	2	$2v$	$-u$
3	27.03	13	5	3	0	u
4	41.54	17	7	4	$2v$	$-u$

An instantaneous snapshot of the turbulence generated in this way is presented in Fig. 3, where the Q-criterion was used to visualize the turbulent structures. The green arrow indicates the mean inlet flow direction and the blue surface denotes the blade surface. The visualized structures appear three-dimensional and random as expected for a turbulent flow. At closer inspection, a pattern of reoccurring structures can be observed in the pitchwise direction. However, the distance between them is sufficiently large (one third of the pitch) that they are not expected to affect the transition behaviour on the blade that is governed by interaction with structures of the size of a few boundary layer thicknesses. To get a more quantitative understanding of the behavior of the background turbulence, a precursor simulation of a rectangular box representing only the inlet region of an LPT cascade setup were conducted, extending from $x = -0.8$ to $x = 1$, where the leading edge of a blade would be located at $x = 0$. Time-spectra of the pitchwise velocity component at different streamwise positions are plotted in Fig. 4. At the inlet ($x = -0.8$), as expected peaks at the introduced wave numbers (given in table 1) are observed. First the small scales develop (high frequencies) and already at 20% chord downstream of the inlet a broadband signal characteristic of a fully turbulent flow is present. Peaks at the injected frequencies are still visible but the gaps are quickly filled and at half a chord length from the inlet the peaks are hardly distinguishable and the spectrum follows the $-5/3$ law. As simulations in the current study have an inlet length of at least 80%

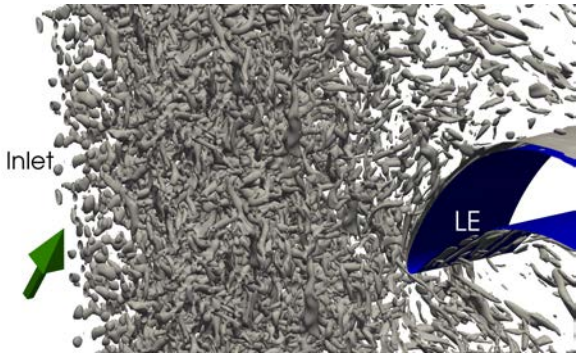

FIGURE 3. STRUCTURES GENERATED USING THE PROPOSED METHOD VISUALIZED USING THE Q-CRITERION AT A LEVEL OF 50.

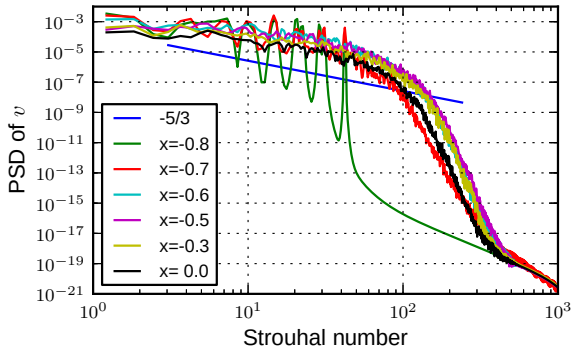

FIGURE 4. TIME SPECTRA AT VARIOUS STREAMWISE POSITIONS WHERE THE LEGEND LABEL IS THE DISTANCE FROM THE INLET.

chord, well developed turbulence will therefore be 'seen' by the blade. Using an autocorrelation function of the time signal and Taylors frozen turbulence assumption, the length scale of the turbulence impacting on the blade has been estimated to be about 5% of chord. Further the decay rate of the turbulence kinetic energy was identified to agree well with experimental data [32] using a decay factor of -1.3. Hence, the required characteristics of the background turbulence, both intensity and length scale, can be obtained using this method.

Sliding Mesh Flows around bodies at motion with respect to one another (e.g. rotor-stator interaction) can be simulated with HiPSTAR using either a moving immersed boundary condition or a sliding mesh. The immersed boundary, whether moving or stationary, is based on the feedback forcing method proposed by Goldstein *et al.* [33] and has recently been shown to accurately represent solid boundaries [34]. The sliding mesh is implemented using a CIC [27] in a moving reference frame. The source and convective terms of the Navier-Stokes equations in characteristic form are evaluated in the reference frame of a neighboring block, and interpolated using the wavenumber-optimized scheme of Tam and Kurbatskii [35]. The same technique can be used to implement patched grids. Advantages of this approach include tolerance of metric discontinuities at the interface, as with the original CIC, and the reduction of the halo

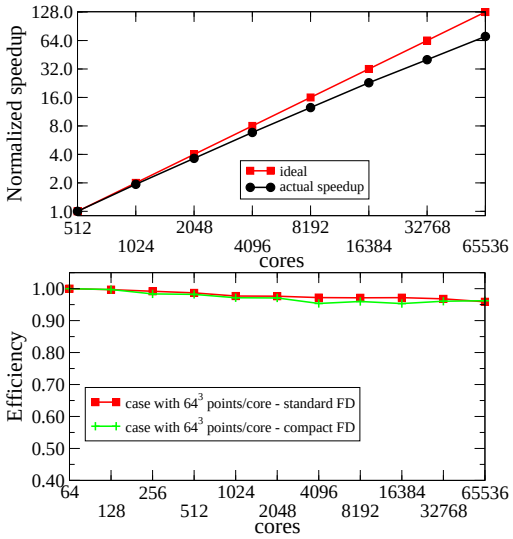

FIGURE 5. STRONG SCALING FOR SINGLE-BLOCK TEST CASE WITH 1 BILLION GRID POINTS ON CRAY XE6 (TOP) AND WEAK SCALING FOR CASES WITH 64^3 GRID POINTS PER CORE ON CRAY XE6 (BOTTOM).

to a single layer of nodes. Flows that are spanwise homogeneous with respect to the mean velocity then require only 1-D interpolation, and this facilitates the use of interpolation schemes that might otherwise be too computationally intensive for DNS. In order to avoid constraining the time step employed by the simulation, a non-blocking consensus algorithm is used for parallelisation, based on that described by Höfler *et al.* [36]. This is used because in absence of such a constraint, block connectivity across the sliding interface can otherwise be subject to roundoff errors. A full description of the method and its validation, both for canonical test cases and for full DNS of linear LPT cascades with incoming wakes, is to be found in Johnstone *et al.* [37]. The accuracy of the new sliding mesh technique is also demonstrated for DNS of an LPT cascade with incoming wakes in the results section below.

Parallelization

To take full advantage of massively parallel HPC systems, the code uses a hybrid OMP/MPI parallelization [38].

Hybrid OMP/MPI CPU version The performance of the DNS code was evaluated on the UK national supercomputing facilities HECToR, a CRAY XE6 architecture, and Blue Joule, an IBM Blue Gene/Q system. Initial scaling tests were performed on HECToR on a single-block test problem with 2048 points in the streamwise and lateral directions, and 128 Fourier modes in the spanwise direction, resulting in a total number of collocation points of 1.08×10^9. In this strong scaling test, i.e. core numbers are varied for a given problem size, the smallest number of cores that could be used was 512, which implies that at least 2.15×10^6 grid points require less than 1Gb of memory and can thus be allocated per core. In Fig. 5 (top) the performance of the code is shown up to 65,536 cores, displaying very good scaling. Weak scaling tests were also performed on single-block

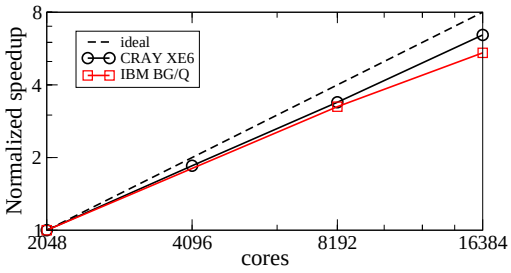

FIGURE 6. STRONG SCALING FOR A NINE-BLOCK LPT CASE WITH 300 MILLION GRID POINTS USING PARALLEL COMPACT FINITE DIFFERENCES WITH CURVILINEAR COORDINATES, USING 2048 MPI PROCESSES AND VARYING THE NUMBER OF OMP THREADS.

test cases, i.e. the number of operations every core has to perform and the MPI messages every core has to send/receive is kept identical for increasing overall number of cores. Fig. 5 (bottom) shows the results from the weak scaling tests for cases with 64^3 grid points per core using the standard and the novel parallel compact finite difference scheme. For both options, the efficiency remains as high as 96% up to 65,536 cores (resulting in a case with 17.2×10^9 grid points). Using 65,536 cores, the time spent per full Runge-Kutta cycle, i.e. five evaluations of the right-hand-side of the governing equations, is 4.87s/step and 5.49s/step for the standard and compact finite difference schemes, respectively. This 13% increase in computational cost of the parallel compact scheme is more than acceptable considering that due to the significantly better wavenumber resolution characteristics of the compact scheme a coarser grid could be used for a given problem. The moderate increase in overall computational time despite the significantly higher algorithmic cost of the compact finite difference schemes can be explained by the fact that codes with better ratios of algorithmic operations (FLOPs) over communication fare better on current bandwidth-limited computing systems.

To evaluate the performance of HiPSTAR for more complex set-ups, a scaling test was performed using the novel parallel compact scheme for a linear low-pressure turbine cascade, in which 9 blocks were connected using characteristic interface conditions to account for metric discontinuities. This performance test was conducted using a grid with approximately 300 million points. Fig. 6 shows that up to 4 OMP threads, the parallel scaling on either system used was comparable. However, at 8 OMP threads, the CRAY system displays a better performance. Overall, the scaling on either system is good for this (real) production-type test case. Finally, it should be noted that in addition to the excellent parallel scaling of the code, the performance of the underlying algorithm also appears to be very good. On the CRAY XE6, a sustained performance of 1 GFLOP/s or 12.5% of peak performance in HiPSTAR's core computation kernels was measured.

To investigate the performance of the code on medium sized clusters that might be more readily available a simulation at an isentropic Reynolds number of 60,000 was conducted on the Intel Xeon based IRIDIS4 cluster at the University of Southampton. Using a moderate number of 476 cores, 5 flow through times

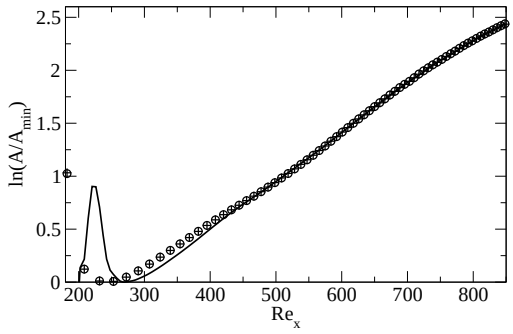

FIGURE 7. AMPLIFICATION RATE OF THE INNER MAXIMUM OF THE STREAMWISE VELOCITY COMPONENT; (—) REFERENCE DNS, (○) HIPSTAR WITHOUT SKEW-SYMMETRIC SPLITTING, (+) HIPSTAR WITH SKEW-SYMMETRIC SPLITTING.

could be obtained in 20 hours. Hence, a full DNS including statistical convergence study would thus take less than 3 days of wall time, or 30,000 core hours.

VALIDATION

A careful validation of HiPSTAR has been conducted. During the development stage, each subroutine was thoroughly tested. Here, only test cases that assess the overall code capabilities are presented.

Instability Waves

The computation of viscous instability growth is a rigorous validation case for near-wall behavior. Initially, Tollmien-Schlichting (TS) waves in a quasi-incompressible boundary layer were simulated and excellent agreement of the growth rate with incompressible reference DNS was obtained, particularly as relatively coarse grid resolutions were used. These simulations were conducted as a Mach number of $M = 0.25$ to minimize the effect of compressibility while still allowing for practical timesteps.

To verify the validity of the spanwise discretization, in particular the Fourier transforms, and the accurate computation of the thermodynamic variables, the growth of oblique disturbances in a supersonic boundary layer at $M = 3.0$ were computed and compared to a reference DNS [39].

The growth rates (Fig. 7) obtained from the current DNS code correspond very well with the data of the reference, except for the region $200 < Re_x < 400$. This deviation most likely arises due to the use of different forcing mechanisms. Mayer *et al.* [39] used wall blowing and suction, whereas the current code employs volume forcing. However, further downstream the agreement with the reference is excellent. When using the skew-symmetric splitting [24] for increased robustness, the non-linear terms are split into conservative and non-conservative parts. To verify that this does not lead to inaccuracies in simulations, an additional DNS was performed using the skew-symmetric splitting. The result is virtually indistinguishable from the initial DNS and gives confidence in the suitability of the skew-symmetric splitting. It should be noted that the skew-symmetric splitting allows larger time-steps, thus improves numerical stability.

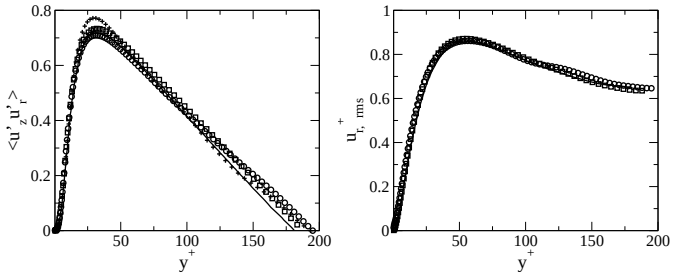

FIGURE 8. TURBULENT SHEAR STRESS $< u_z' u_r' >$ (LEFT) AND RMS OF THE RADIAL VELOCITY FLUCTUATIONS $\sqrt{< u_r' u_r' >}$ (RIGHT) AS A FUNCTION OF $y^+ = (1-r)^+$; (—) REFERENCE DNS [41], (□) HIPSTAR PERIODIC SET-UP, (○) HIPSTAR SPATIAL SET-UP WITH TURBULENT INFLOW CONDITION.

Turbulent Pipe flow

Turbulent pipe flow was simulated in order to validate the code for fully turbulent flow and its cylindrical coordinate capability with a novel axis treatment [40]. Streamwise periodic calculations were first carried out at Mach number $M = 0.4$ and Reynolds number $Re = 5,300$, based on pipe diameter and bulk velocity in order to compare with recent data [41]. Following Wu and Moin [41], the length of the pipe was set to $L_p = 15R$, and 201×72 grid points were used in the streamwise and radial directions, respectively, and 64 Fourier modes in the azimuthal direction. Grid points were uniformly distributed in the streamwise periodic direction, while a polynomial stretching was used in the radial direction with maximum and minimum grid spacings $\Delta r = 0.025R$ and $\Delta r = 0.00246R$ at the axis ($r = 0$) and wall ($r = R$), respectively. Further, DNS were computed for a spatially developing turbulent pipe flow. In this case, the same radial grid was used as in the periodic case, but the streamwise length of $L_p = 50R$ was discretized with 624 grid points. For the inflow boundary condition, a digital filter technique for inflow turbulence generation [30] was employed, using the required mean flow profiles, integral length scales and Reynolds stress distributions from the periodic DNS. In Fig. 8 the turbulent shear stress and the root-mean-square of radial velocity fluctuations obtained with HiPSTAR from both set-ups are compared to the reference data. Statistical data obtained from the periodic DNS was averaged in both the axial and azimuthal directions, while the data from the spatially developing case was averaged only in the azimuth and taken 45 radii downstream of the inlet. The current DNS results are in excellent agreement with the benchmark data.

In addition to these rigorous test cases, the DNS code has recently been used for DNS of turbulent supersonic wakes [42] and turbulent jets issuing into coflow [43] for analysis of jet noise.

Linear Low-Pressure Turbine Cascade

Although HiPSTAR has been thoroughly validated for a range of flows and the code is now in routine use for DNS studies of turbulent flows and aerodynamically generated noise, its suitability for high-fidelity simulation of low-pressure turbine cascades remains to be demonstrated. The turbine blade geometry considered in the current work is the T106 profile experi-

mentally investigated by Stadtmüller [44]. The measurements were obtained in a low-pressure linear turbine test rig with seven aft-loaded blades with an aspect ratio of 1.76, implying that the flow at the midspan can be considered to be statistically two-dimensional. Therefore, the use of spanwise periodic boundary conditions would appear to be a reasonable assumption. In the experiments, the pitch-to-chord ratio, stagger angle λ, the inlet flow angle β_1 and the exit flow angle β_2 are 0.799, 30.7°, 37.7° and 63.2°, respectively. However, as explained in Michelassi *et al.* [45], there is some uncertainty about the actual inlet conditions, both in terms of total pressure and inlet flow angle, and an inlet angle of 45.5°, based on RANS and incompressible DNS, was suggested. Incompressible simulations of compressible measurements generally yield anticipated and stronger peak suction, as observed by Wissink [21]. To overcome this problem, the current simulations are performed with a compressible fluid at the experimental Mach number. Further to this, the inlet flow angle was fine-tuned to 46.1 deg [31] to reproduce the blade load in the immediate proximity of the leading edge.

A variable density system in the test rig allowed measurements at a relatively low isentropic exit Reynolds number of 60,500 and an isentropic exit Mach number of 0.4. In the current study, the resulting Reynolds number and Mach number were 59,634 and 0.405, respectively. Additionally a case at same Mach number but with an isentropic exit Reynolds number of 100,000 was simulated. In all cases the ratio of specific heats is specified as $\gamma = 1.4$ and the Prandtl number as $Pr = 0.72$. The spanwise width of the computational domain was chosen as 0.2 chord lengths, which is deemed to be sufficient to capture transition in a possibly separated blade boundary layer based on previous experience gained with separation bubbles on low-Reynolds number aerofoils [18]. Furthermore, previous studies of linear turbine cascades found a spanwise width based on axial chord of 0.2 [21] or even 0.15 [19] to be adequate. The spanwise domain was discretized using 32 Fourier modes with 100% de-aliasing (resulting in 66 collocation points). For the lower Reynolds number case the number of grid points along the surface of the blade is 864 points and in the wall normal direction the spacing is nearly constant around the blade with $\Delta y = 2.8 \times 10^{-4}$ and 336 points spanning the blade passage in the pitchwise direction. Thus, the overall number of grid points of the DNS is 18.1×10^6.

The first wall-normal grid point on the suction side is located at $y_1^+ < 1$ for most of the pressure side and for the suction side downstream of 60% chord. Upstream of that, the maximum value is below 1.4 which, given that the boundary layer is laminar and in excess of 30 points are used across the boundary layer, is deemed sufficient. The resolutions in the streamwise and spanwise directions are $\Delta x^+ < 10$ and $\Delta z^+ < 11$, similar to the values used in the incompressible DNS by Michelassi *et al.* [45]. A nondimensional timestep of $t = 5 \times 10^{-5}$ was specified in order to satisfy the numerical stability requirement of a CFL number of less than unity.

For the DNS at an isentropic exit Reynolds number of $Re_{2is} = 100,000$, the baseline grid comprised 1296 grid points along the blade and 526 points in the pitchwise direction, resulting in the first off-the wall point being at $\Delta y = 1.5 \times 10^{-4}$. 64 Fourier modes were used for the spanwise discretization leading to a total of 75.6×10^6 grid points. The grid resolution in the streamwise and spanwise directions are $\Delta x^+ < 11$ and $\Delta z^+ < 9$ and the wall normal resolution is presented in Fig. 9. The blue solid line denotes the baseline grid and the dashed green line represents a finer grid refined by roughly a factor of two in each direction, resulting in a total of about 300×10^6 grid points. The first cell y^+ for both grids is less than unity, except for the regions close to the leading and trailing edges. Close to the leading and trailing edges y^+ on the suction side displays two zero crossings, indicating separation with subsequent reattachment. The chordwise locations of these zero crossings coincide for both grids, suggesting that the boundary layers and particularly transition in the trailing-edge separation are fully resolved on either grid, i.e. grid convergence is reached about the blade. The DNS at $Re_{2is} = 60,000$ were performed using 3808 cores, requiring 16-20 hours for 15 flow-through-times, resulting in a total of 60,000 core hours on a CRAY XE6. At $Re_{2is} = 100,000$, 8080 cores were used for 72 hours for 15 flow-through-times, expending a total of 582,000 core hours per case on the IBM BlueGene/Q.

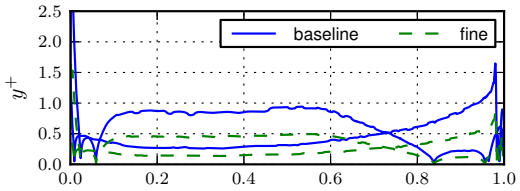

FIGURE 9. DISTANCE OF FIRST OFF-THE-WALL GRID POINT IN WALL UNITS FOR DNS AT $Re_{2is} = 100,000$.

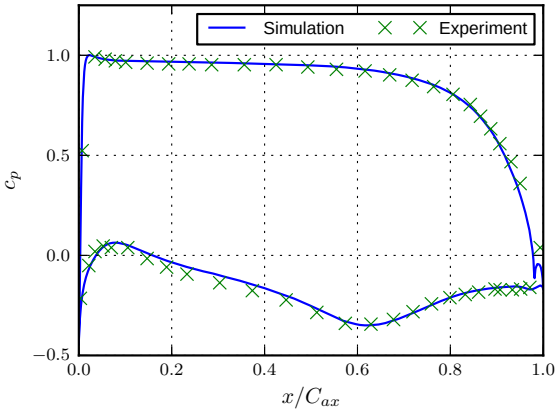

FIGURE 10. PRESSURE COEFFICIENT ON BLADE COMPARED WITH EXPERIMENTS [44] FOR CASE WITH $Re_{2is} = 60,000$.

For the $Re_{2is} = 60,000$ case, the pressure distribution about the blade is compared with experimental results [44]. On the pressure side the DNS results show excellent agreement with the experimental data. Peak suction is found slightly further downstream than in the experiment which might be due to boundary layer growth and the related blockage at the end walls in the experiments. Of particular interest in this study is the behavior downstream of peak suction where separation and reattachment dictate the pressure coefficient shape. In this region experiments and simulation are in close agreement.

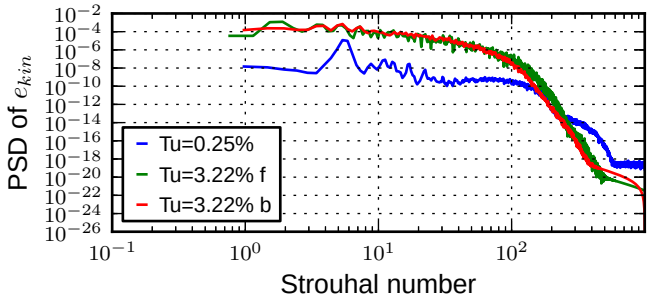

FIGURE 11. SPECTRA OF TURBULENT KINETIC ENERGY IN THE INLET REGION FOR CLEAN AND TURBULENT CASES AT RE=60,000.

A good agreement of the blade pressure coefficient does not necessarily mean that the entire computational domain is adequately resolved, in particular the wake region. Therefore, wake profiles at a vertical section 40% chord downstream of the trailing edge are investigated. First, DNS were conducted with 'clean' inlet conditions, i.e. no incoming wakes and zero turbulence level at the inlet. As will be shown in the following, the use of a compressible DNS solver represents an additional challenge on the inlet and outlet boundary conditions which artificially truncate the physical flow field to not generate spurious reflections, in particular for clean inflow conditions. At the outlet boundary characteristic or zonal characteristic boundary conditions [46] are employed. At the inlet boundary, a sponge layer, based on adding a dissipation term to the right-hand side of the governing equations, forcing the flow solution to a target state [47], was implemented [31]. In Fig. 11 the power spectral density of kinetic energy at the measurement point in the inlet region is shown for a clean case. Considering that no turbulence is injected at the inlet, the fluctuation level, although small, has to stem from other sources. A significant part of this energy is attributed to upstream traveling acoustic waves generated by hydrodynamic pressure fluctuations interacting with the blade trailing edge. The main peak in the spectrum is at a Strouhal number (reference values are free stream velocity and chord length) of about 5, suggesting it may be associated with low-frequency unsteadiness of the suction side separation bubble. A lower amplitude peak at a Strouhal number of 15 reflects the vortex shedding at the trailing edge.

These low-amplitude acoustic fluctuations can be seen in Fig. 12 (top) where the divergence of the velocity field is plotted. Using the local speed of sound, the wave-length of perturbations with a Strouhal number of 5 can be estimated to be approximately 0.7 chords, which agrees well with what can be seen in the figure. The contour levels reach zero in the inlet sponge region indicating that no disturbances reach the inlet boundary. As a reference and to further motivate the use of a sponge layer, the divergence field of a simulation that was conducted without a sponge is presented in Fig. 12 (bottom). Note that in this figure the contour levels are a factor of 10 higher than in the case with sponge. High-amplitude acoustic waves populate the entire domain, with the largest amplitude waves traveling in the pitchwise direction and resulting in large inlet perturbation levels in an instantaneous and statistical sense [31]. Therefore, this set-up has

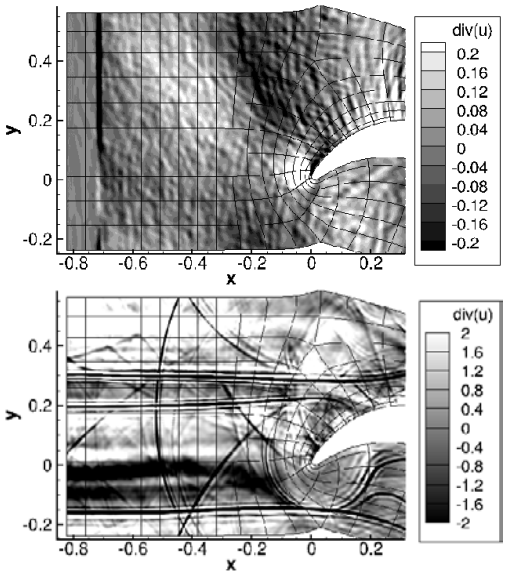

FIGURE 12. DIVERGENCE OF THE VELOCITY FIELD FOR CLEAN INFLOW CASES AT $Re_{2is} = 60,000$ WITH (TOP) AND WITHOUT (BOTTOM) SPONGE AT INLET.

not been further considered in the current work.

Overall, it is found that the disturbance level of the clean case when using an effective sponge is at roughly 0.25%, caused by acoustic fluctuations. In the experiment the hydrodynamic fluctuation level is 0.6% and thus significantly higher. Our study reveals that this difference in inflow disturbance levels has a significant impact on the wake loss and comparing experiments at 'clean' conditions with simulations is far from trivial. The wake losses from the DNS and experiments are compared in Fig. 13 . The clean experiment and the simulation with the lowest level of disturbance level (0.25%) do not agree well but if the fluctuation level at the inlet is increased to roughly the same value as in the experiments (0.5%), the DNS data agree well with the experiments.

Although the integrated wake loss between the cases with disturbance level of 0.25% and 0.5% are very similar at 0.0628 and 0.0615, respectively, the change of the peak value and shape is surprisingly large and implies that the wake loss shows significant dependence on inlet turbulence levels even for different disturbance levels below 1%. Therefore, if DNS data are to be compared with experiments classified as 'clean', the precise disturbance characteristics present in the experiments need to be known and replicated in the DNS in order for results to agree.

Additionally, two more cases at a more realistic engine-like turbulence intensity of 3.2% were conducted at $Re_{2is} = 60,000$ on the baseline (denoted by 'b') and a refined grid (denoted by 'f'). The power spectral density of the kinetic energy for both grids agree well with each other, as seen in Fig. 11, indicating that the turbulence generation method is grid independent and the baseline grid is sufficiently fine to resolve the incoming background turbulence adequately. The figure also reveals that the background turbulence at realistic engine conditions is several orders of magnitude higher than the spurious disturbances discussed above. Crucially, the wake loss for the DNS with dis-

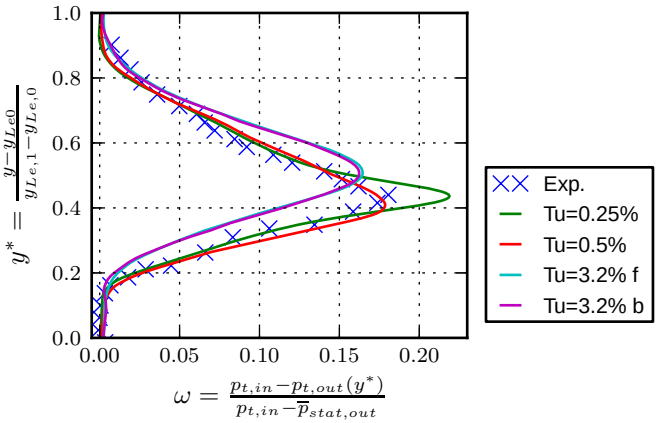

FIGURE 13. WAKE LOSS COMPARED WITH EXPERIMENTS [44] AND GRID CONVERGENCE STUDY FOR $Re_{2is} = 60,000$.

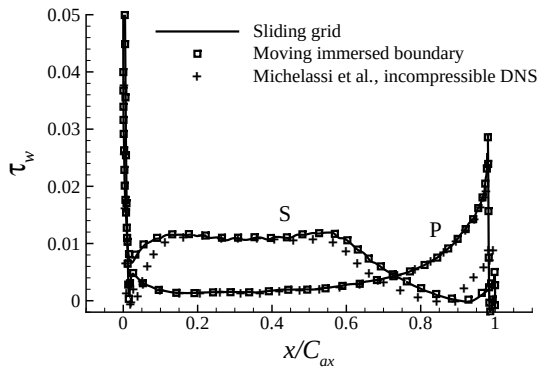

FIGURE 14. WALL SHEAR STRESS; DNS OF T-106A CASCADE WITH INCOMING WAKES AT A REDUCED FREQUENCY $F_{RED} = 0.61$, GENERATED BY SIMULATING THE BARS BY TWO DIFFERENT METHODS, COMPARED TO INCOMPRESSIBLE DNS DATA [20]. P=PRESSURE SIDE, S=SUCTION SIDE OF THE BLADE.

turbance level at 3.2% appears grid independent, validating the baseline grid and overall set-up.

Finally, DNS of T106 blades at a chord and exit velocity Reynolds number of 60,000 and the exit Mach number 0.4 were performed with incoming wakes at a reduced frequency, i.e. frequency of the bars normalized by chord and isentropic exit velocity, of 0.61. The wakes were generated by including moving bars realized by an immersed boundary in the computational domain. Full details about the numerical set-up and the immersed boundary for the moving bar cases are given in Part II of this paper and in Johnstone *et al.* [37]. For the current study, two approaches for moving the bars were compared. In one case, a fixed grid is used and the immersed boundary is moved. In the other case, the immersed boundary is fixed relative to the grid of the upstream block and the entire block slides relative to the downstream blade. Both simulations were run up to statistical convergence. Fig. 14 shows the wall shear stress on both suction and pressure surfaces of the blade, obtained using both the moving immersed boundary and the sliding mesh methods. The results are virtually indistinguishable, demonstrating the accuracy of the novel approach of realizing a sliding mesh based on characteristic interface conditions. The current DNS results are also compared with the incompressible DNS data of Michelassi *et al.* [20]. On the pressure side of the blade, the comparison between the current DNS and the reference is excellent. The wall shear-stress level agrees well with the incompressible DNS for $0.2 \lesssim x/C_{ax} \lesssim 0.45$. Upstream of that, the differences observed are due to the difference in inlet angle which results from including the wake generating bars in the current simulations while in the incompressible reference case wakes were inserted at the inlet boundary. For the remaining section of the blade, the data from the current DNS appear shifted downstream by approximately 0.05 x/C_{ax} but agree very well in shape. This is due to the shift in peak suction location between incompressible and compressible DNS, as already observed for the cases without incoming wakes. It is important to note that this shift in peak suction also results in a change of the chordwise length over which the flow experiences an adverse pressure gradient, which directly affects the loss generation mechanisms.

CONCLUSION

A high-performance compressible Navier–Stokes solver developed for exploiting the latest computing hardware and adapted to conduct direct numerical simulations of linear low-pressure turbine cascades has been presented and thoroughly validated. A novel approach of implementing a sliding mesh capability for DNS was introduced and an efficient way of introducing background turbulence was presented. It is demonstrated that DNS of LPT at moderate Reynolds number can be accomplished in reasonably short time, e.g. within a day for Re=60,000, thus opening the door for using DNS to conduct parameter sweeps, as will be reported in part II of this paper. Also, it is found that in order to obtain the correct adverse pressure gradient downstream of the suction peak on the blade, both in terms of magnitude and chordwise length, it is essential to use compressible DNS. Further, it is shown that the wake loss is highly sensitive to inlet turbulence levels even at disturbance levels below 1% and that even the disturbance level of 'clean' experiments needs to be known and replicated in DNS in order to match the experimental data. As very low background turbulence levels are unlikely to occur in real engine configurations, it is suggested that validation between DNS and experiments would be more reliable for turbulence levels above 1% as otherwise the results depend too strongly on boundary conditions.

ACKNOWLEDGMENT

The first author acknowledges financial support through a Royal Academy of Engineering/EPSRC research fellowship (EP/E504035/1). Computing time on the U.K.'s national supercomputing service HECToR (CRAY XE6) was provided by the UK turbulence consortium under EPSRC Grant EP/G069581/1, and time on the IBM Blue Gene Q was provided by the STFC Hartree Centre.

REFERENCES

[1] Mayle, R. E., 1991. "The role of laminar-turbulent transition in gas turbine engines". *J. Turbomachinery,* ***113***(4), pp. 509–537.

[2] Halstead, D., Wisler, D., Okiishi, T., Walker, G., Hodson, H., and Shin, H.-W., 1997. "Boundary layer development in axial compressors and turbines: Part 1 of 4 - Composite picture". *J. Turbomachinery,* ***119***(1), pp. 114–127.

[3] Engber, M., and Fottner, L., 1996. "The effect of incoming wakes on boundary layer transition of a highly loaded turbine cascade". In AGARD CONFERENCE PROCEEDINGS, AGARD.

[4] Hodson, H. P., and Howell, R. J., 2005. "Bladerow interactions, transition, and high-lift aerofoils in low-pressure turbines". *Annu. Rev. Fluid Mech.,* ***37***, pp. 71–98.

[5] Heinke, W., König, S., Matyschok, B., Stoffel, B., Fiala, A., and Heinig, K., 2004. "Experimental investigations on steady wake effects in a high-lift turbine cascade". *Experiments in Fluids,* ***37***(4), pp. 488–496.

[6] Keadle, K., and McQuilling, M., 2013. "Evaluation of RANS transition modeling for high lift LPT flows at low Reynolds number". In ASME Turboexpo, GT2013-95069, ASME.

[7] Raverdy, B., Mary, I., Sagaut, P., and Liamis, N., 2003. "High-resolution large-eddy simulation of flow around low-pressure turbine blade". *AIAA J.,* ***41***(3), pp. 390–397.

[8] Matsuura, K., and Kato, C., 2006. "Large-eddy simulation of compressible transitional cascade flows with and without incoming free-stream turbulence". *JSME Intern. J. Series B,* ***49***(3), pp. 660–669.

[9] Sarkar, S., 2009. "Influence of wake structure on unsteady flow in a low pressure turbine blade passage". *J. Turbomachinery,* ***131***(4).

[10] Medic, G., and Sharma, O. P., 2012. "Large-eddy simulation of flow in a low-pressure turbine cascade". In ASME Turboexpo, GT2012-68878, ASME.

[11] Michelassi, V., Wissink, J., Fröhlich, J., and Rodi, W., 2003. "Large-eddy simulation of flow around low-pressure turbine blade with incoming wakes". *AIAA J.,* ***41***(11), pp. 2143–2156.

[12] Kim, J., Moin, P., and Moser, R., 1987. "Turbulence statistics in fully developed channel flow at low reynolds number". *J. Fluid Mech.,* ***177***, pp. 133–166.

[13] Spalart, P., and Allmaras, S., 1992. "A One-Equation Turbulence Model for Aerodynamic Flows". *AIAA Paper 92–0439*, Jan. 30th AIAA Aerospace Sciences Meeting, Reno, USA.

[14] Davidson, P. A., 2004. *Turbulence: An Introduction for Scientists and Engineers*. Oxford University Press.

[15] Moin, P., and Mahesh, K., 1998. "DIRECT NUMERICAL SIMULATION: A Tool in Turbulence Research". *Ann. Rev. Fluid Mech.,* ***30***(1), pp. 539–578.

[16] Alam, M., and Sandham, N. D., 2000. "Direct numerical simulation of 'short' laminar separation bubbles with turbulent reattachment". *J. Fluid Mech.,* ***403***, pp. 223–250.

[17] Spalart, P., and Strelets, M., 2000. "Mechanisms of transition and heat transfer in a separation bubble". *J. Fluid Mech.,* ***403***, pp. 329–349.

[18] Jones, L. E., Sandberg, R., and Sandham, N., 2008. "Direct numerical simulations of forced and unforced separation bubbles on an airfoil at incidence". *J. Fluid Mech.,* ***602***, pp. 175–207.

[19] Wu, X., and Durbin, P., 2001. "Evidence of longitudinal vortices evolved from distorted wakes in a turbine passage". *J. Fluid Mech.,* ***446***, pp. 199–228.

[20] Michelassi, V., Wissink, J., and Rodi, W., 2003. "Direct numerical simulation, large eddy simulation and unsteady Reynolds-averaged Navier-Stokes simulations of periodic unsteady flow in a low-pressure turbine cascade: A comparison". *Proc. IMechE, Part A: J. Power and Energy,* ***217***(4), pp. 403–411.

[21] Wissink, J., 2003. "DNS of separating, low Reynolds number flow in a turbine cascade with incoming wakes". *Int. J. Heat Fl.,* ***24***(4), pp. 626–635.

[22] Wissink, J., and Rodi, W., 2006. "Direct numerical simulation of flow and heat transfer in a turbine cascade with incoming wakes". *J. Fluid Mech.,* ***569***, pp. 209–247.

[23] Kennedy, C., Carpenter, M., and Lewis, R., 2000. "Low-storage, explicit Runge–Kutta schemes for the compressible Navier–Stokes equations". *Appl. Num. Math.,* ***35***, pp. 177–219.

[24] Kennedy, C., and Gruber, A., 2008. "Reduced aliasing formulations of the convective terms within the Navier–Stokes equations for a compressible fluid". *J. Comp. Phys.,* ***227***, pp. 1676–1700.

[25] White, F. M., 1991. *Viscous Fluid Flow*. McGraw Hill.

[26] Kim, J., and Sandberg, R., 2012. "Efficient parallel computing with a compact finite difference scheme". *Computers & Fluids,* ***58***, pp. 70–87.

[27] Kim, J., and Lee, D., 2003. "Characteristic Interface Conditions for Multiblock High-Order Computation on Singular Structured Grid". *AIAA Journal,* ***41***(12), pp. 2341–2348.

[28] Michálek, J., Monaldi, M., and Arts, T., 2012. "Aerodynamic Performance of a Very High Lift Low Pressure Turbine Airfoil (T106C) at Low Reynolds and High Mach Number With Effect of Free Stream Turbulence Intensity". *Journal of Turbomachinery,* ***134***(6), p. 061009.

[29] Tabor, G., and Baba-Ahmadi, M., 2010. "Inlet conditions for large eddy simulation: A review". *Computers and Fluids,* ***39***(4), pp. 553–567.

[30] Touber, E., and Sandham, N., 2009. "Large-eddy simulation of low-frequency unsteadiness in a turbulent shock-induced separation bubble". *Theor. Comp. Fluid Dyn.,* ***23***(2), pp. 79–107.

[31] Sandberg, R., Pichler, R., and Chen, L., 2012. "Assessing the sensitivity of turbine cascade flow to inflow disturbances using direct numerical simulation". In 13th International Symposium for Unsteady Aerodynamics, Aeroacoustics and Aeroelasticity in Turbomachinery (ISUAAAT).

[32] Comte-Bellot, G., and Corrsin, S., 1966. "The use of a contraction to improve the isotropy of grid-generated turbulence". *J. Fluid Mech.,* ***25***(4), pp. 657–682.

[33] Goldstein, D., Handler, R., and Sirovich, L., 1993. "Modeling a no-slip flow boundary with an external force field". *J. Comp. Phys.,* ***105***, pp. 354–366.

[34] Schlanderer, S. C., and Sandberg, R. D., 2013. "DNS of a Compliant Trailing Edge Flow". *AIAA Paper 2013–2013*.

[35] Tam, C., and Kurbatskii, K., 2000. "A wavenumber based extrapolation and interpolation method for use in conjunction with high-order finite difference schemes.". *J. Comp. Phys.,* ***147***, pp. 588–617.

[36] Höfler, T., Siebert, C., and Lumsdaine, A., 2010. "Scalable communication protocols for dynamic sparse data exchange.". In 2010 ACM SIGPLAN Symposium on Principles and Practice of Parallel Programming (PPoPP'10), ACM, pp. 159–168.

[37] Johnstone, R., Chen, L., and Sandberg, R. A sliding characteristic interface condition for direct numerical simulations. Submitted to *Computers and Fluids*.

[38] Edwards, T., and Sandberg, R. D., 2011. "Cray centre of excellence project report 2011". In www.hector.ac.uk/coe/pdf/HiPSTAR_OMP_Report.pdf.

[39] Mayer, C. S., von Terzi, D. A., and Fasel, H. F., 2011. "Direct numerical simulation of complete transition to turbulence via oblique breakdown at Mach 3". *J. Fluid Mech.,* ***674***, pp. 5–42.

[40] Sandberg, R. D., 2011. "An axis treatment for flow equations in cylindrical coordinates based on parity conditions". *Computers and Fluids,* ***49***, pp. 166–172.

[41] Wu, X., and Moin, P., 2008. "A direct numerical simulation study on the mean velocity characteristics in turbulent pipe flow". *J. Fluid Mech.,* ***608***, pp. 81–112.

[42] Sandberg, R. D., 2012. "Numerical investigation of turbulent supersonic axisymmetric wakes". *J. Fluid Mech.,* ***702***, pp. 488–520.

[43] Sandberg, R., Suponitsky, V., and Sandham, N., 2012. "DNS of compressible pipe flow exiting into a coflow". *Int. J. Heat Fluid Fl.,* ***35***, pp. 33–44. DOI: 10.1016/j.ijheatfluidflow.2012.01.006.

[44] Stadtmüller, P., 2001. "Investigation of Wake-Induced Transition on the LP Turbine Cascade T106 A-EIZ". *DFG-Verbundprojekt Fo 136/11,* ***Version 1.0***. , University of the Armed Forces Munich, Germany.

[45] Michelassi, V., Wissink, J., and Rodi, W., 2002. "Analysis of dns and les of flow in a low pressure turbine cascade with incoming wakes and comparison with experiments". *Flow, Turbul. Combust.,* ***69***(3-4), pp. 295–329.

[46] Sandberg, R. D., and Sandham, N. D., 2006. "Nonreflecting zonal characteristic boundary condition for direct numerical simulation of aerodynamic sound". *AIAA J.,* ***44***(2), February, pp. 402–405.

[47] Freund, J., 1997. "Proposed inflow/outflow boundary condition for direct computation of aerodynamic sound". *AIAA J.,* ***35***(4), pp. 740–742.